International Journal of Physical Sciences

Volume 9 Number 10 30 May, 2014
ISSN 1992-1950

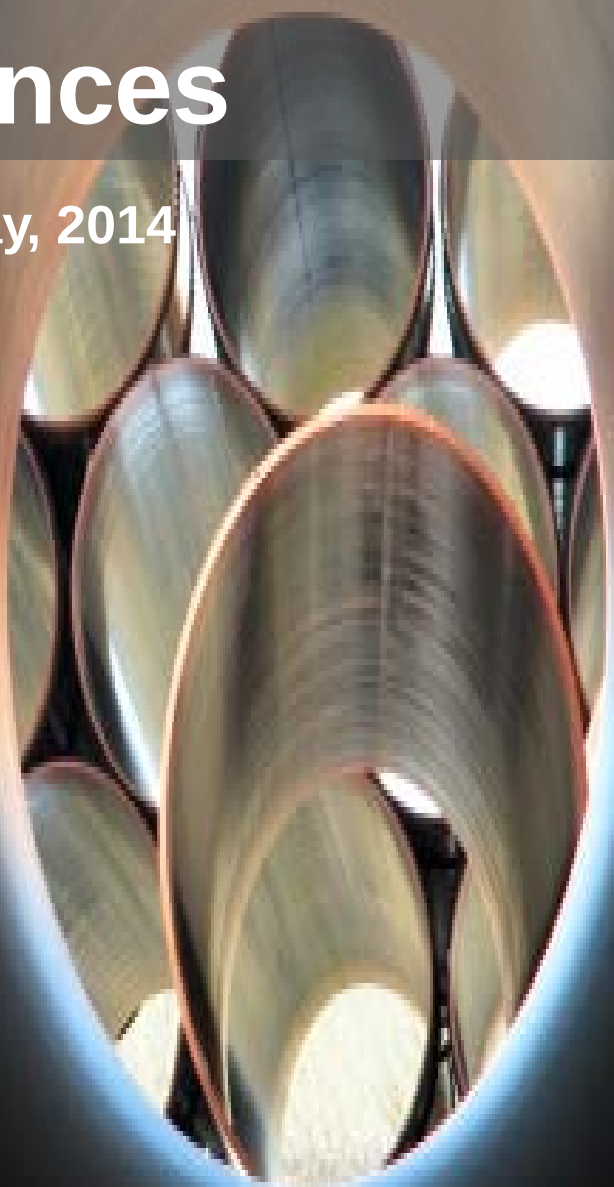

Academic Journals

ABOUT IJPS

The **International Journal of Physical Sciences (IJPS)** is published weekly (one volume per year) by Academic Journals.

International Journal of Physical Sciences (IJPS) is an open access journal that publishes high-quality solicited and unsolicited articles, in English, in all Physics and chemistry including artificial intelligence, neural processing, nuclear and particle physics, geophysics, physics in medicine and biology, plasma physics, semiconductor science and technology, wireless and optical communications, materials science, energy and fuels, environmental science and technology, combinatorial chemistry, natural products, molecular therapeutics, geochemistry, cement and concrete research, metallurgy, crystallography and computer-aided materials design. All articles published in IJPS are peer-reviewed.

Contact Us

Editorial Office: ijps@academicjournals.org

Help Desk: helpdesk@academicjournals.org

Website: http://www.academicjournals.org/journal/IJPS

Submit manuscript online http://ms.academicjournals.me/

Editorial Board

International Journal of Physical Sciences

Table of Contents: Volume 9 Number 10, 30 May, 2014

ARTICLES

Study of vibrations by Raman spectroscopy low frequencies of the phase transition in pyridinium picrate ($C_6H_2N_3O_7$)-.(C_5H_6N)$^+$ 233
AZIZI Abdelkader and MEDDOUR Athmane

Analysis and supervision of the water extraction of a thermal power plant 243
M. N. Lakhoua

Simulation analysis of the effect graded Zn(O,S) on the performance of the ultra thin copper indium gallium diselenide (CIGS) solar cells 250
Chihi Adel, Boujmil Mohamed Fethi and Bessais Brahim

academicJournals

Vol. 9(10), pp. 233-242, 30 May, 2014
DOI: 10.5897/IJPS2013.4084
Article Number:776F63545011
ISSN 1992 - 1950

http://www.academicjournals.org/IJPS

International Journal of Physical Sciences

Full Length Research Paper

Study of vibrations by Raman spectroscopy low frequencies of the phase transition in pyridinium picrate $(C_6H_2N_3O_7)^-.(C_5H_6N)^+$

AZIZI Abdelkader* and MEDDOUR Athmane

Department of Physics, Faculty of M. I. S. M, 08 May 1945 University, BP 401, Guelma 24000, Algeria.

Received 02 December, 2013 ; Accepted 14 February, 2014

The spectra of the crystals of pyridine picrate crude formula, $C_{11}H_8N_4O_7$, in the mid infrared (IR) and Raman are studied as a function of temperature. They show some changes, which allowed us to first track and describe the structural changes (in both directions under the effect of heat treatment) accompanying the phase transition between 358 and 383K observed by DSC, Rx. After gradual cooling, the reversibility of the alteration may be detected by the variation 1'etude frequencies and relative heights of the lines connected to groups of bands NO_2, NH and CH. The results show that the transformation kinetics is influenced by the operational conditions.

Key words: Picrate pyridine transition phase, reversibility, infrared (IR), Raman, X-ray diffraction (XRD).

INTRODUCTION

Pyridinium picrate has properties which make it useful in various fields such as biology, optics, catalysis; it is also used for purification in the pharmaceutical industry. Hence, it is necessary to know the importance of the thermal stability of the two phases or the polymorphic behavior of the active substance in order to optimize operation and storage conditions so that only the desired shape is seen in the processes.

This work contributes to the study of phenomena related to the dimorphic of an organic salt called 'picrate pyridine' $[(C_6H_2N_3O_7)^-.(C_5H_6N)^+]$ by comparing the behavior of its two forms, named Phases I and II, respectively. This is done to provide additional structural and spectral data to previous results of other authors, by monitoring the behavior and activity of any group of spectroscopy essential for the understanding of its mechanism of structural changes in order to address the question of reversibility of this transition. To do this, a particular technique was preferred: Raman spectroscopy. It has the ability to provide guests with information on the molecule structure, its binding mode and the presence or absence of an interaction; this makes particular interesting target to be influenced by particular groupings of transition phase phenomena. This works aims to complement the studies of the structural data of this dimorphic. This is because till date, there is no comprehensive study on the vibration spectra of crystals, PicPy. The unusual work is essentially based on X-ray diffraction (XRD), which we made reference to in this study (Botoshansky et al., 1994; Talukdar and Chaudhuri, 1976).

*Corresponding author. E-mail: azizikader@yahoo.fr

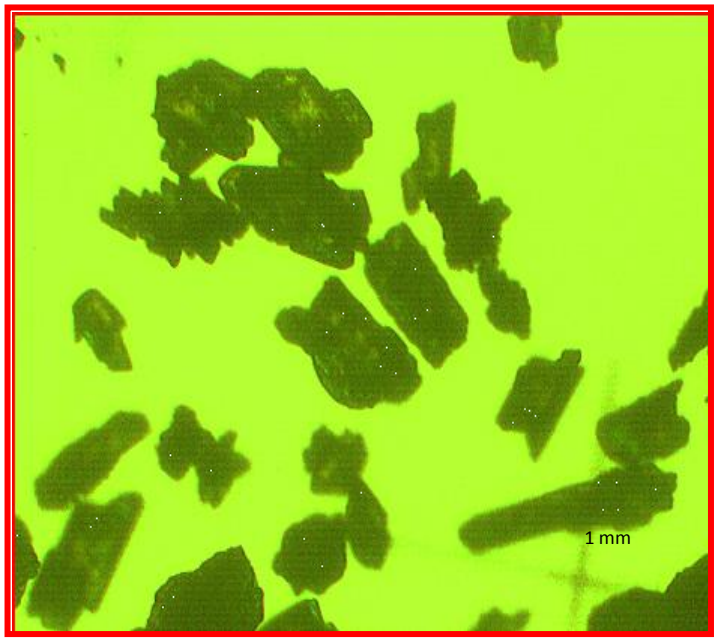

Figure 1. Micrograph of crystals ambient (yellow).

EXPERIMENTAL DETAILS

Synthesis and preparation of crystals

The synthesis powder was made by precipitation. This involves slow evaporation of saturated solution of a stoichiometric mixed with reagents (202 g of picric acid and 0.8 g of pyridine). Yellow crystals that stain were grown after being filtered in a vacuum and then were weighed. 204 g of crystals with a yield of 97% (precipitation rate) was obtained. This product is stable and can be handled in open air without any special precautions. The micrograph of the crystal analysis (Figure 1) shows that the product obtained does not have very regular form, but the major fraction of the population of these crystals has an average size of 0.9 × 0.8 × 0.04 mm^3.

It is already remarked that during the preparation, the crystals change color when exposed to relatively high temperatures of around 363K (boiling solvent) for about 10 min. The coloration of the crystals changes from light yellow to brown. The same color change was observed by Mark et al. (1994).

Thermal analysis by differential scanning calorimetry

For structural characterization, it is very important to start with the study of thermal behavior in order to identify areas of stability and transition, highlight thermal anomalies revealing any change in these properties under the influence of the thermal environment. For this purpose, we used first thermal analysis by differential scanning calorimeter.

The curves were obtained on a sail Labsys Evo TG- DSC, with a mass of 35 mg of sample in an aluminum crucible and in a measuring cell with a capsule called a reference. They were subjected to a temperature program ranging from 293 to 424K, as ramps 285, 283 and 281K/min under nitrogen atmosphere (35 ml/min). These curves (Figure 2) show that at the beginning of 358K, thermal activity gives rise to a first endothermic peak center of 368K, which is the melting starting point of Phase I, followed by an exothermic peak intermediate between the two bands (endothermic), which combine a recrystallisation solution Phase II with a second endothermic peak at 383K. The melting peak does not appear on the curve, being a limited temperature of 423K. This is done to prevent degradation of the product in the device and thus damaging its smooth operation.

In both endothermic points, the hypothesis of the formation of Phase II, following the merger of Phase I at the same temperature (358K) is given by Mark et al. (1994) and Talukdar and Chaudhuri (1976); this gave us an idea of the areas in which the temperatures must focus on for XRD, infrared (IR) and Raman records. It is noted that the recordings done by cooling the samples at these speeds show no sign of activity.

Diffraction X -ray powder (XRD)

To control the structure, it is ensured that the compounds prepared in the expected system are well crystallized. Two samples were prepared; one was stored at room temperature (293K) and the other treated in an oven at a temperature of 368K for 30 min (in order to cause the transition phase). They were characterized by XRD using a diffract meter operating with copper Kα radiation (λ = 1.5406 Å). The records obtained are shown in Figure 3.

The indexing of the experimental peaks of diffractograms was done by using the program Mercury CCDC and ASTM (02-068-1154). The refinement of the cell parameters of Phase I (at room temperature) shows that it crystallizes in a monoclinic system, space group $P2_{(1)/c}$, with lattice parameters,

a = 12.122(2) Å; b = 3.7830(10) Å; c = 26.621(3) Å;
α = 90°; β = 92.56°(5); γ = 90° et Z = 4, Z' = 4.

and at the processing temperature of 368K for 30 min (the transition Stage II) in a triclinic system, space group P-1 with cell parameters:

a = 10.156(2) Å; b = 8.984(2) Å; c = 7.2300(10) Å ;
α = 86.38(5)°; β = 80.10(5)°; γ = 89.97(5)° et Z = 2, Z' = 0.

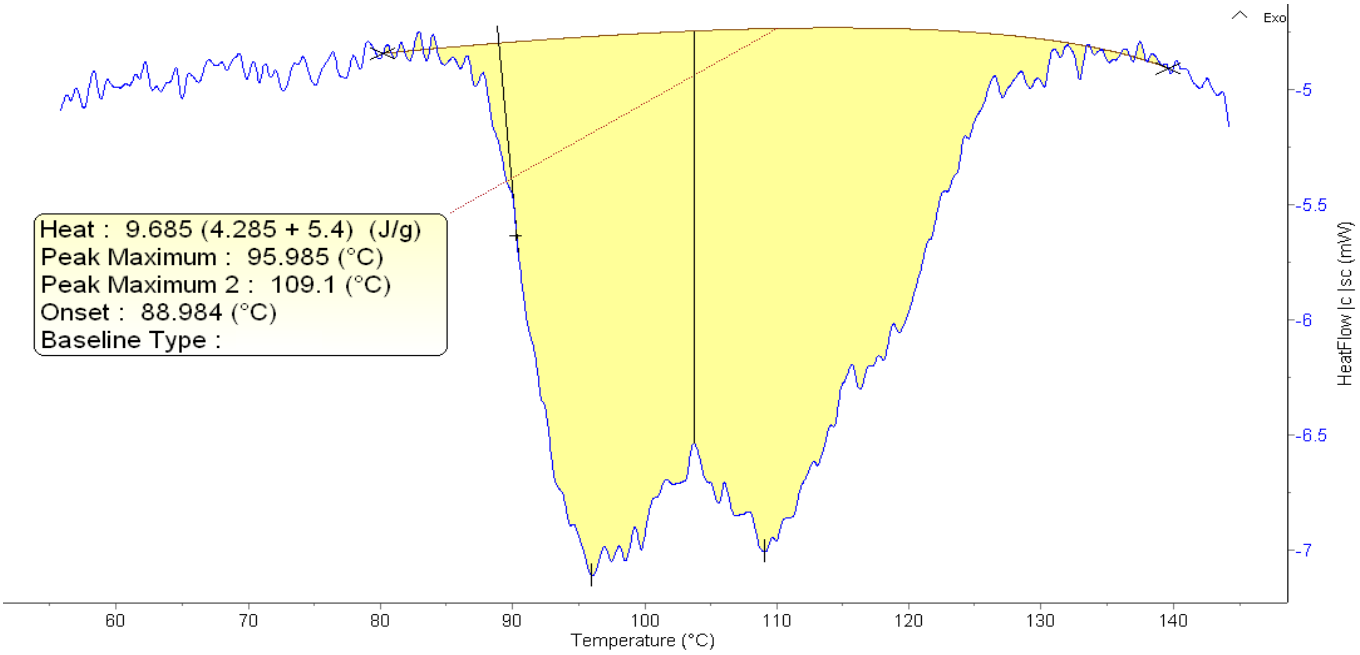

Figure 2. DSC thermograms.

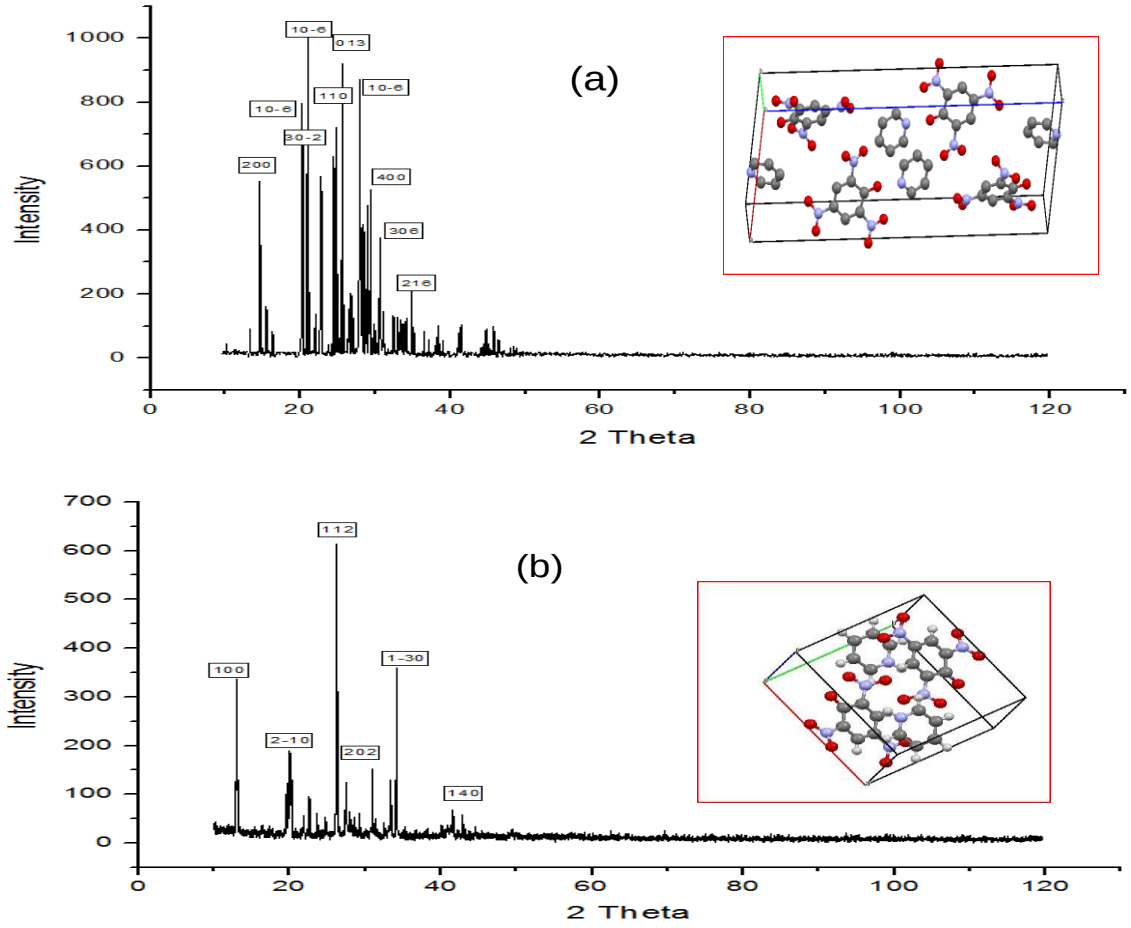

Figure 3. XRD diffractograms of the samples treated for 30 min at temperature **(a),** 298K; **(b),** 368K.

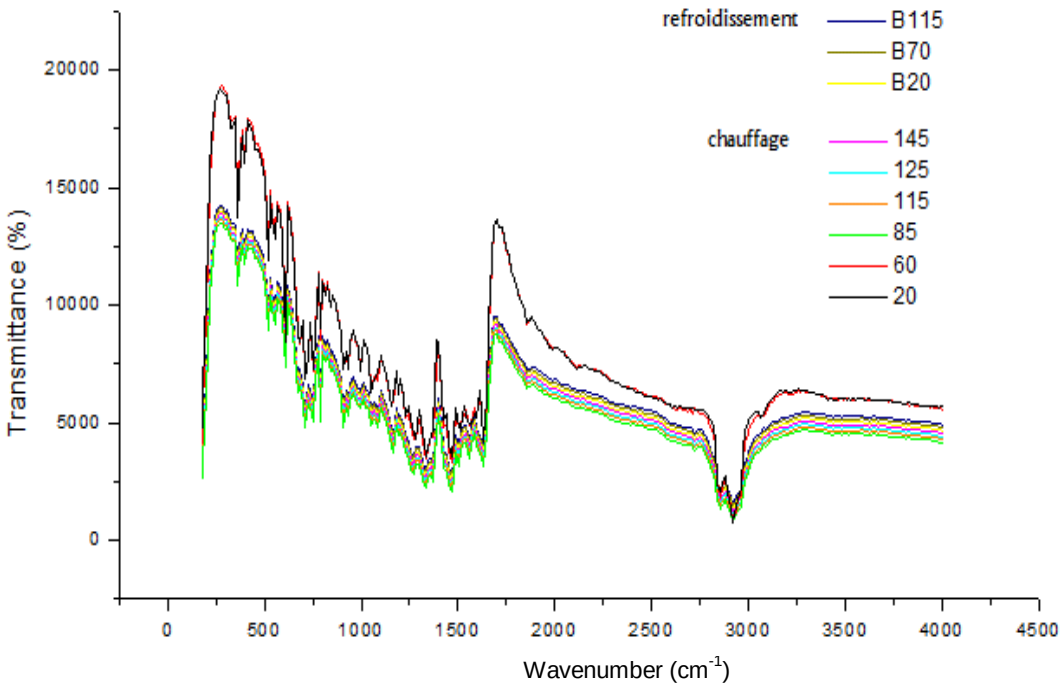

Figure 4. Influence of temperature on the IR transmission spectra 293, 333, 358.398 and 418K (During heating); B115 and B388, B343 and B29 (during cooling).

RESULTS AND DISCUSSION

Vibrational spectroscopic study

IR and Raman spectroscopy recorded as a function of temperature (and time), the frequency domain initially scanned and the samples are in the form of powder in suspension in Nujol. To monitor the behavior and check the reversibility of the process of phase transition upon cooling, IR spectra were recorded on heating at temperatures going from ambient to 418K (293, 333, 358.398 and 418K); but during gradual cooling, the temperatures were lowered (B388, B343 and B293). The aim is to record spectra at critical temperatures, where we observed the thermal anomalies on the DSC curves. Figure 4 shows the transmittance spectra.

In general, we observe two sets of parallel spectra with the same speed and bands. The spectra recorded at 293 and 333K are very similar and they fit perfectly. So we think that there is no change. However, at 358K, the spectra are slightly modified compared to those recorded at lower temperatures; and beyond 358K, the recordings are also almost identical with that recorded at 388, 398 and 418K. However, there are differences between the massive 600 and 800 cm^{-1}, around 1450 cm^{-1} and 1350 cm^{-1} and between 1400 and 1750 cm^{-1}.

At 388K, there is a remarkable evolution of the spectra; there is contrast reversal of intensities between 600 and 400 cm^{-1}; we note that the number of bands decreased for regions between 850 to 750 cm^{-1} and 1350 to 1750 cm^{-1}.

Attempting IR bands award

The complexity of the crystal structures of the complete assignment makes each PicPy very delicate peak. In comparison with previous work and studies conducted on similar complexes and databases in the literature, it was possible to assign most of the peaks. Table 1 summarizes the main groupings.

IR spectra composed were compared with the Raman spectra (Figure 5) based on the thermal variations or anomalous thermal survey on the DSC curves and on the basis of two XRD diffractgrams. The spectra are shown in Figure 6 for two temperatures: ambient (raw sample) and 368K. The vibration spectra show much mark than the IR spectroscopy with 368K temperature differences. We note that bands are fewer and have more specific characteristics and locations.

It is evident that the spectra consist of two frequency ranges, with changes of matter; spectral region between 110 to 1500 cm^{-1} mode field elongation CC bonds and strain CN 1140 to 1180 cm^{-1} field user elongation CC bonds. Fine deformation peak is recognized in the planes of the groups NO_2 and 820 cm^{-1}, which is observed with no decrease in the intensity change of position (Varsanyi, 1974).

The strips 711 (IR) and 721 cm^{-1} (R) have very low intensity of vibration in the plane deformation of C-H bonds; the rocking vibration in the nuclei is observed at 912 cm^{-1}. The CC stretching vibrations of the cycle are relatively small and are located at 1592, 1506, 1460 (IR),

Table 1. Summary of the main award bands (Varsanyi, 1974; Silverstein et al., 1991; George Socrates, 2004; Roeges, 1994)

Frequency (cm^{-1})		Attribution
Phase I	**Phase II**	
3095	3080	v C-H ring str
1631	1630	v C-C ring str
1571 1555	1563 1553	v asym NO_2
1486 1477	1506 1461	v C-C ring
1365 1346	1367 1345	v sym NO_2
1283	1266	v phen C-O
- 822	837 819	δ NO_2
742	745	NO_2 wag.
695	678	γ_w C-C
516	514	γ NO_2

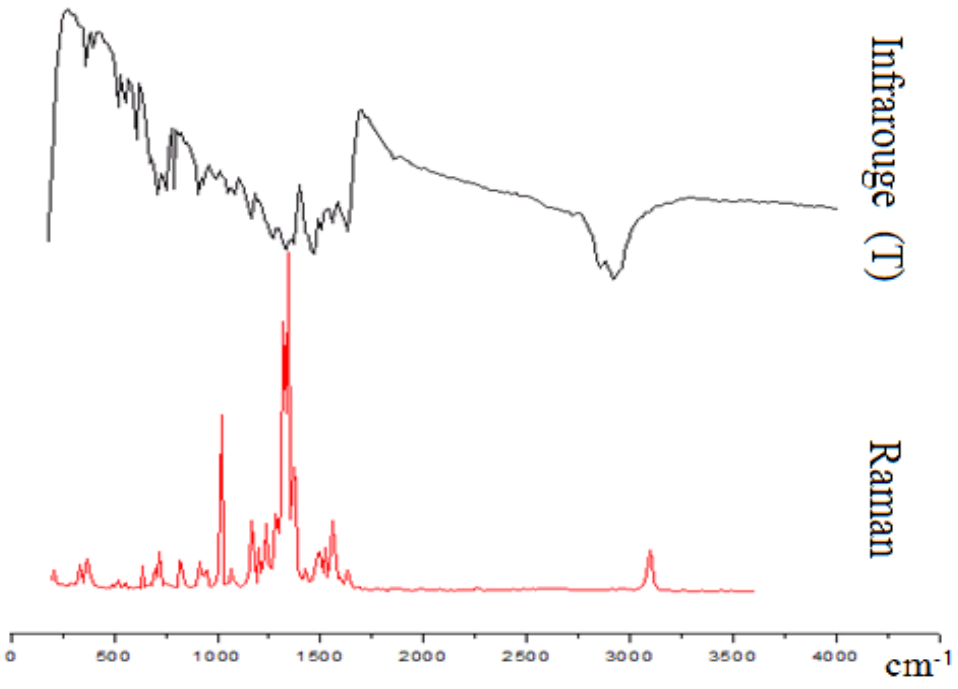

Figure 5. Comparison of IR and Raman spectra PicPy 293K.

1477 (R) cm^{-1} and bending modes between 690 and 730 cm^{-1}. Other modes of deformation are observed by a small band of 1266, 1073, 1018, 1000 and 786 cm^{-1} (Silverstein et al., 1991; George Socrates, 2001).

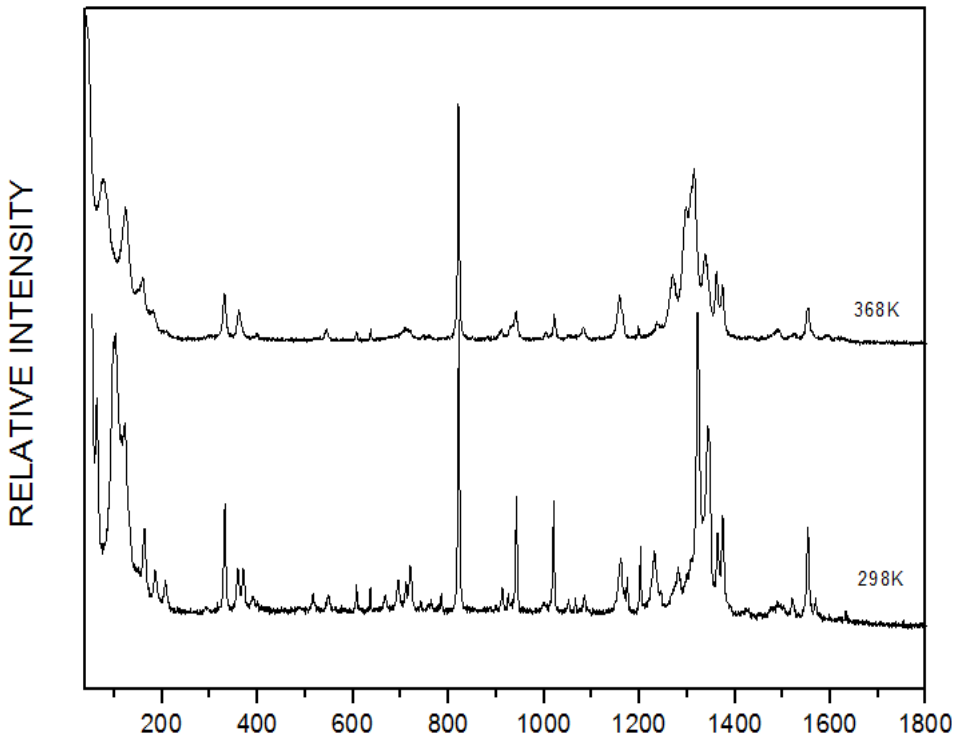

Figure 6. Raman spectra for two temperatures 298 and 368K.

Duplication of core bands around 360 cm^{-1} is assigned to the stretching vibration mode of the CNC pyridine. The position of these bands is fixed and the intensity is greatly changed. Because the intense and broad absorption is centered around 1325 cm^{-1} with several shoulders, this mass slides, by effect of temperature and its width, decreases considerably with several shifts of these peaks. These shifts cause changes in the spectroscopic band profile and intensity, gang evolution with temperature and a shift towards lower frequencies of the Raman band at 796 cm^{-1}; elongation binding depending on the temperature, and the opening angle between the cation-anion to the low wave numbers where collective movements occur (Gunter and Tuan, 2008; Kalsi, 2004).

ANALYSIS BY RAMAN SPECTROSCOPY (LOW FREQUENCY MODES)

In Raman spectrometry, in particular, lower region of less than 250 cm^{-1} frequency, and said network users (external or modes) that are due to the movements of translation and rotation of the molecules in the crystal lattice are bands stretching vibrations (CH and L.H. groups) that are very sensitive to intra-and intermolecular arrangement, as amended within and outside plane of the ring and vibration of aromatic rings themselves. For this purpose, recordings are made on Raman spectroscopy of the samples in sealed tubes, using an excitation wavelength of 1.06 microns (IR), obtained with a laser having an output of 60 mW in the laser output, a spectral between 05 and 4000 $cm^{-1.}$

Raman spectra as a function of temperature

A. During heating

Raman registered for different temperatures (Figure 6) spectra clearly shows the existence of two distinct crystalline forms (Phases I and II), previously identified by XRD patterns (Figure 3); in some disturbance vibration modes reflection, one notices a structural change or transition. Figure 7 shows the shape of the spectra and their changes as a function of increasing temperature in a range going from 298 to 443K records on heating and cooling (Varsanyi, 1974; Silverstein et al., 1991).

The Raman spectra (Figure 7a) are mainly composed of two stage types. In the first, there is a series of fine and intense peaks below 75 cm^{-1}, located at 22, 30, 50 and 63 cm^{-1}. They are mostly due to movements involving more groups in the form of couplings (torsion deformation). The few internal vibrations of relatively high frequency are also detected in the form of relatively broad bands, a second region composed of higher frequencies by two broad bands at 100 and 123 $cm^{-1,}$ in shoulder form with small secondary strips at 164, 186, and 205 cm^{-1}.

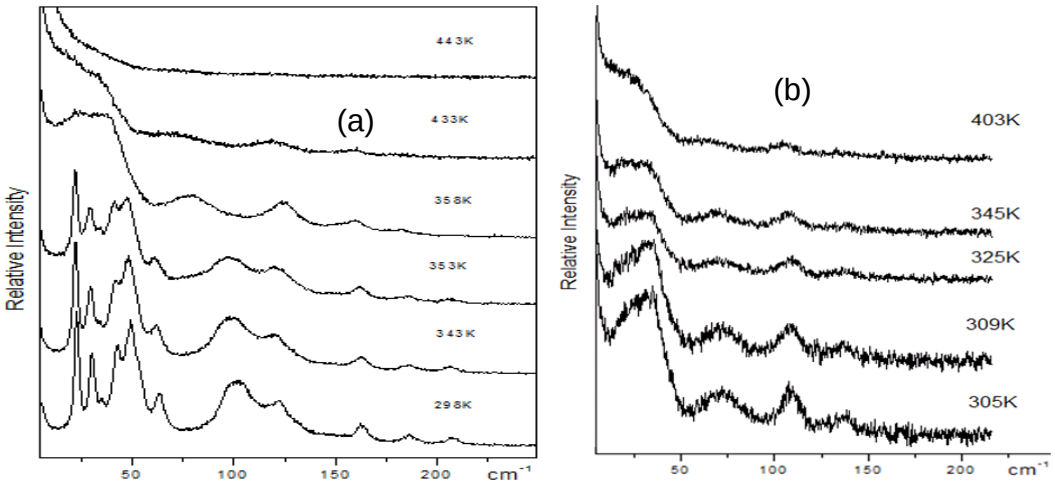

Figure 7. Raman spectra at different temperatures (low frequencies) (a) heating (b) cooling.

Table 2. Assignment of low frequency modes.

Frequency (cm^{-1})	Attribution
22.5	-
30	-
35.2	-
40-50-60	τ NO_2
100	L.H , *δs*(CH)
120	γ (C-C-C)
165	β(C-NO2)
186	β(C-O),
205	β(C-NO_2)

ν: Elongation; **β, γ:** deformation dans et hors plan; **γ_w:** balancement hors plan.

These secondary peaks disappear during increase in temperature (beyond 353K). We note the changing profile of the main lines of the first region, which is seen to expand and form a broad bump with total recovery. Remember that bump is called the amorphous specific Boson. Also, two interesting bands at 60 and 100 cm^{-1} give rise to a weak band center of 75 cm^{-1}; extremely weak bands (Figure 7b) and small bands of 164, 186 and 205 cm^{-1} tend to disappear (or vice- versa tape). The observed frequencies and their allocation are reported in Table 2. This development is interpreted by steric effects and structural deformation and then by the transition from monoclinic to triclinic structure.

B. During cooling

Spectra have also been recorded during cooling, at the following temperatures: 403, 345, 325, 309 and 305K. The obtained recordings are represented in Figure 4b. They always appear in Structure II with side bands of 300, 200 and 120 cm^{-1} and whose intensity is inversely with changes in temperature. Furthermore, we note the emergence of a wide strip resulting recovery bands is 37 cm^{-1}. This means that the phenomenon of transition dimorphic is not irreversible to Phases II and I (in these operating conditions). At the end, at 433 and 443K temperatures, melting resulted in the complete absence of peaks.

The crystal structure through the main lines keeps up the temperature of 353K (80°C) and then forms a large mass center at 40 cm^{-1}, which has a smooth assignment of the structural arrangement. In fact, when the temperature increases, there is distortion of the crystalline structure by displacement of the frequencies of vibrations in the direction of decreasing the angle between cation-anion through hydrogen bonding. This is less rigid, thus reducing the vibration frequency of hydrogen bond. As shown in Figure 7a, b, it is from 100 cm^{-1} for 293K and 75 cm^{-1} for 403K

Profiles of some parameters

Figure 8 illustrates the information in the changing frequencies of the lines of the Raman spectra as a function of temperature. In the first movement, it is found that V1 to V4 modes have no frequency that is substantially stable (frequency is insensitive due to temperature). On the other hand, the higher frequency mode has a slight growth with a problem of bending to around 345K; band is denoted as V6; they pass about 64 cm^{-1} at 289K to 100 cm^{-1} at 353K. This shift results from all disturbances which bring structural changes.

Then, the intensity of these lines varies inversely with temperature, but with a large difference between the slopes (the attenuation bands). V5 and V7 modes show a

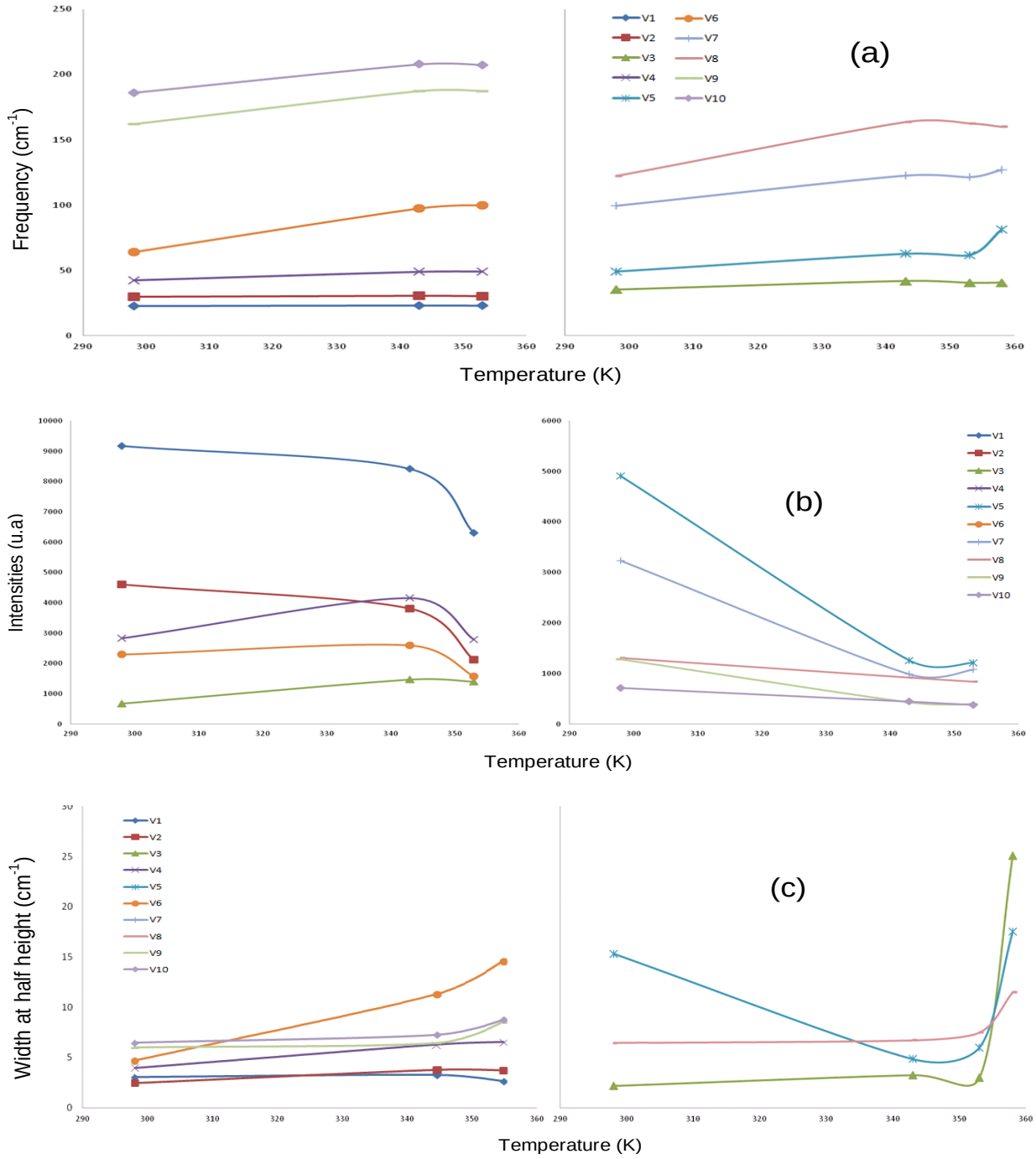

Figure 8. Variation in function of the temperature (a) Frequency (b) intensities and (c) the width at half height of the different modes (<250 cm^{-1}).

great decrease in the frequencies between 300 and 340K; this reduction becomes relatively less pronounced in modes V1 and V4, when the temperature is above 340K; other modes decrease almost linearly with a slope change in the vicinity of the same temperature. Figure 8c illustrates the monitoring of the behavior of the width at half height of the peaks depending on the temperature. It is noted that this parameter varies little in absolute value in terms of peak low frequency V1, V2 and V4 with a variation of about 5 cm^{-1}. This is unlike that of the V5 and V3 modes, wherein the width at half height of the peaks shows a rapid increase with enlargement of the passage and temperature of 350K. An inflection point is observed with a more rapid increase. These parameters are full

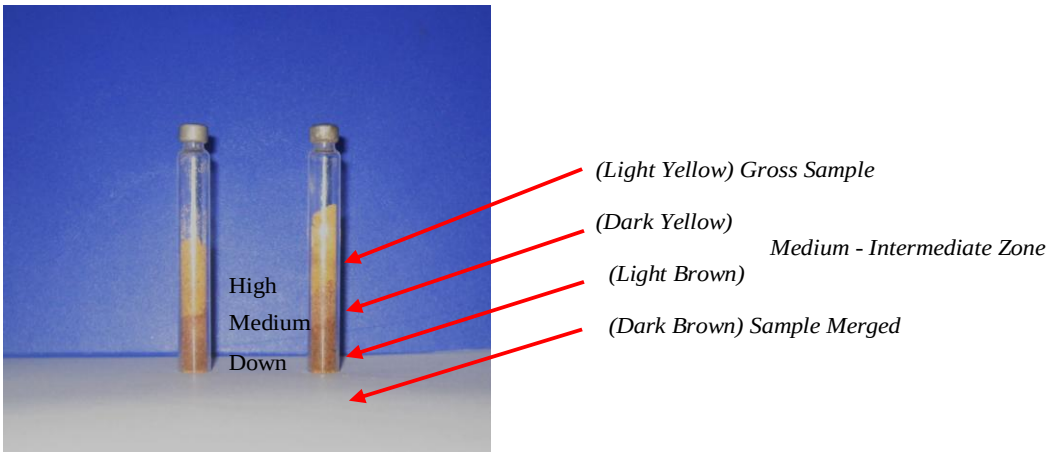

Figure 9. Sealed tubes brought to fusion at their end in a furnace.

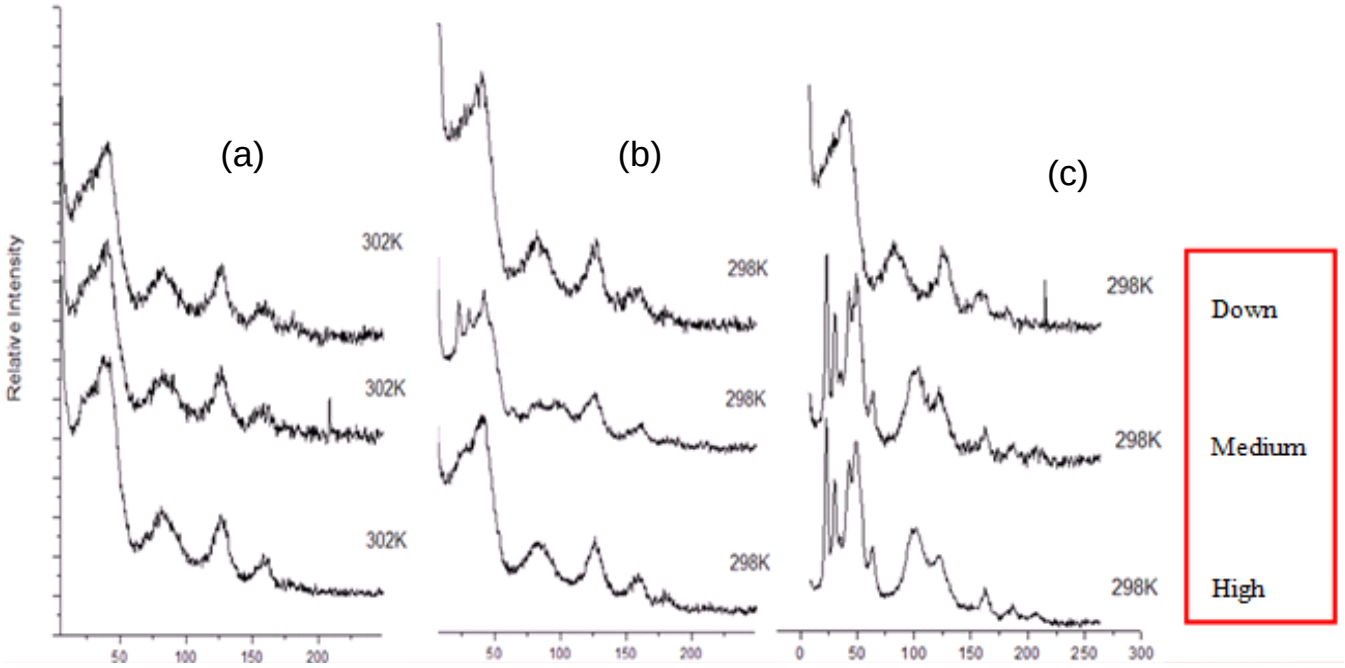

Figure 10. Evolution of the Raman spectra as a function of time (constant temperature), after 30 min (b) after 24 h (c) after 48 h.

information, particularly sensitive to the nature of the arrangements and connections. These abnormalities affecting the variation width at half height and the variation mode V5 frequencies are indicative of the existence of a phase transition at a temperature of about 345K.

Study of the evolution of the Raman spectra of time

Figure 9 shows the samples having different zones formed after treatment of the lower end of tube (sealed) in an oven at 443K for 30 min.

In general, the structure is retained when the room temperature (between 293 and 303K) is kept for a while and going up after 24 h (Figure 10a and b); by cons, it changes structure involved in the case where the sample is held in the sealed tube for a period of 48 h (Figure 10c). It is now apparent that the spectra have the same lines, speeds and equal intensity that start the sample 47 (a) at lower temperature (353K) almost together. Under these conditions, there is crystallization of Phases I in Phase II.

The Raman spectroscopy in Figure 11 demonstrates the reversibility of the phenomenon of transition. That is to say, in the recovery of the structure of the Phase I, the

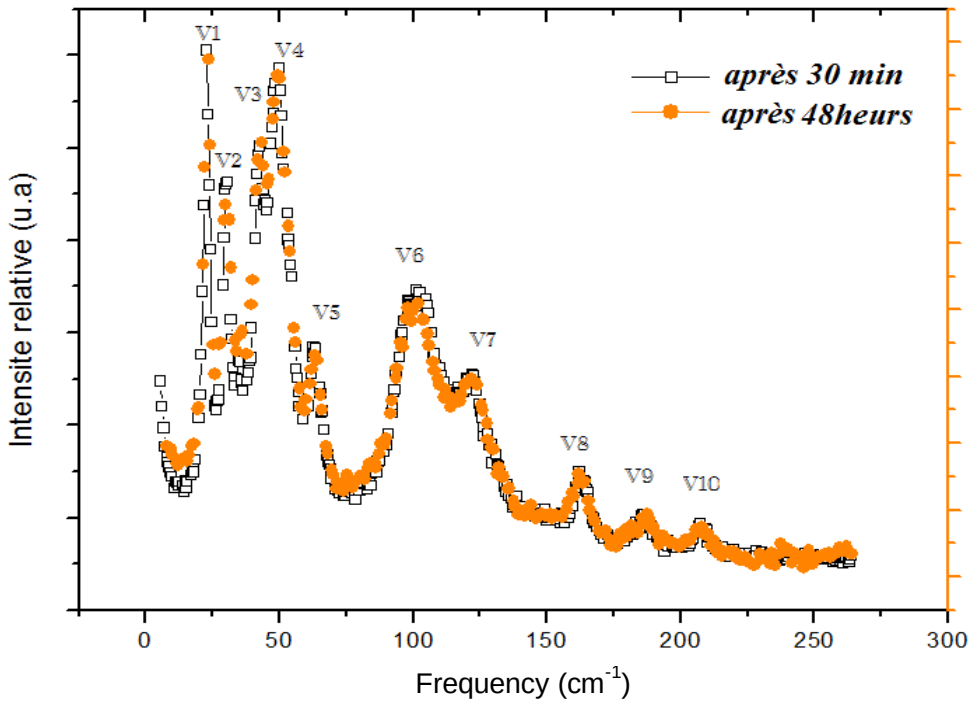

Figure 11. Comparison of the spectra of a sample before treatment and after treatment 433K.

two spectra, in fact, the crude sample was kept ambient and the other at 30 min and 48 h. They were maintained in the cell after the ambient undergoes treatment at 433K (170°C); they are identical and fit perfectly in position and intensity.

Conclusion

This study provides useful information on the nature of the transition and structural relaxation mechanism; in particular, those related to NO_2 groups, NH and CH, involved during the transition. We have discussed the relationship between the internal and phase transition mode, the dependence of frequency width at mid-height and the intensity of the band, depending on the temperature, with a common point in the immediate vicinity of 360K. There are signs of 1'existence of structural change. This affects both mode networks (external mode) and the internal vibration modes. However, in the second part of this study, after gradual cooling of the sample and holding for several hours (48 h) at room temperature, the time required for relaxation is the presence of reversibility, as evidenced by the reappearance of the strips. After relaxation under these operating conditions, the spectra of form I do not evolve with time.

Conflict of Interests

The authors have not declared any conflict of interests.

REFERENCES

Botoshansky M, Herbstein FH, Kapon M (1994). Pyridinium picrate - the structures of phases I and II. Correction of previous report for phase I. Acta Crystallographica, Section B. 50:191-200. http://dx.doi.org/10.1107/S0108768193008584

George Socrates (2001). Infrared and Raman characteristic group frequencies table and chartes. Wiley: Middlesex, UK.

Gunter G, Tuan VD (2008). Handbook of Spectroscopy. Volume 1. pp. 39-45; 100-110.

Kalsi PS (2004). Spectroscopy of Organic Compounds new age international publishers 6TH edition.pp. 87-162.

Mark B, Frank HH, Moshe K (1994). Crystallography of metal picrates. II. Crystal structure of yellow thallium(I) picrate; relations among various M(I) picrate phases. Acta Cryst. B50:589-596. http://dx.doi.org/10.1107/S0108768194001746

Roeges NPG (1994). A guide to the complete interpretation of infrared spectra of organic structures, Wiley: New York.

Silverstein RM, Bassler GC, MORRILL TC (1991). Spectrometric Identification of Organic Compounds 5th Ed. John Wiley. New York. 1991.

Talukdar AN, Chaudhuri B (1976). The crystal and molecular structure of pyridine picrate. Acta Cryst. B32:803. http://dx.doi.org/10.1107/S056774087600397X

Varsanyi G (1974). Assignments of vibrational spectra of seven hundred benzene derivatives, Wiley: New York.

academicJournals

Vol. 9(10), pp. 243-249, 30 May, 2014
DOI: 10.5897/IJPS12.299
ISSN 1992 - 1950
Article Number :E13023B45013

http://www.academicjournals.org/IJPS

International Journal of Physical Sciences

Full Length Research Paper

Analysis and supervision of the water extraction of a thermal power plant

M. N. Lakhoua

University of Carthage, UR: Mechatronics Systems and Signals, ESTI, Tunis, Tunisia.

Received 8 April, 2012; Accepted 24 February, 2014

The aim of this paper is to analysis the water treatment process in a thermal power plant (TPP). In fact, we present an application of a supervisory control and data acquisition (SCADA) system. Thus, an example of a SCADA system of the center of RADES in Tunisia was presented. Our contribution in this work consists in the analysis of the water loss in the TPP on the one hand and the supervision of the water extraction circuit using the SCADA system, on the other hand.

Key words: Water extraction, water loss; thermal power plant, supervisory control and data acquisition (SCADA).

INTRODUCTION

Every day, we use the electric energy without even to be conscious of it. The electric energy serves in all domains including those where we think that it is not used (central heating of gas, thermal motor-driven vehicles...). Means of production of this energy are very various; we classify them today depending on whether they are based on renewable energies or fossil energies. With regards to these last, reserves not being inexhaustible, we tries to replace them by the renewable energies that have for main advantage to be less polluting.

The Tunisian Society of Electricity and Gas (STEG) is a society whose main function is to produce electricity in order to satisfy needs of its customers. Among electricity production centers of the STEG, we mention the center of RADES (near to Tunis, Tunisia) (Annual Report, 2012). It is one of the most important centers of the point of view the power installed (700 MWS). It has been inaugurated in 30 of May, 1986. It is about a thermal power plant (TPP) producing electricity while using dry water steam to drag the alternator in rotation, this steam is generated in a furnace that transforms the chemical energy of the fuel (natural gas, heavy fuel-oil) in calorific energy. By reason of the complex requirements and in order to avoid the maximum loss of production, it is extremely important to master all aspects having linked to the security and the profitability of the highest level.

In fact, the electricity production in a TPP is based on a set of energies transformations using water as support of energy. This water must have a noble quality in order to guarantee the installation security and to improve production groups' performances. It is therefore necessary to apply a rigorous water treatment and a control of its quality (Vitaly, 2008).

The process of the electricity production in the TPP of RADES is essentially based on the water distributed by the SONEDE (National Water Distribution Utility of

E-mail: MohamedNajeh.Lakhoua@enit.rnu.tn

Tunisia). This water generally contains dissolved mineral salts and organic matters. The presence of these elements can generate problems bound to the furring, the corrosion and the different facilities contamination notably the furnace, the steam-powered turbine and water or steam circuits (Kagiannas et al., 2003; Ecob et al., 1995).

In order to assure the required quality of water in the water-steam cycle of the TPP, the water treatment process is necessary. Indeed, water passes by the filtration chain then introduced in the inverse osmosis station and thereafter in the demineralization station (Changling and Boon-Teck, 2006). In fact, the water of the SONEDE used in the TPP of RADES is unfit to the feeding of furnaces. It contains matters suspended and in various solutions in nature and in quantity of salts and gases dissolved. The matter suspended is constituted of the sand, of colloidal clays, insoluble mineral salts and of organic matters (products of animal and plant deterioration). These bodies give a certain coloration to water (turbidity) that requires a clarification treatment. This undesirable foulness can drive to the serious damages. Among which we mention notably corrosion and furring (or encrustations). In order to avoid these problems, it is necessary to:

(i) Eliminate gases (CO_2, O_2, N_2) of the water by the physical degassing or the chemical degassing by the injection of the oxygen reduction as N_2H_4…
(ii) Use of the destitute water of mineral salts for example water done demineralization with a conductivity ($\sigma < 0.2$ µS/cm) and a content in silica $SiO_2 < 30$ ppb.
(iii) Work with a sufficiently basic pH ($8.5 < pH < 9.5$).

The objective of this paper is to identify the water loss in a TPP and to control the water extraction circuit using a SCADA system. An example of a SCADA system of the TPP of RADES is presented.

PRESENTATION OF AN EXAMPLE OF A SCADA SYSTEM

The supervisory control and data acquisition (SCADA) term refers to a system that collects data coming from different sensors of an industrial or other process, these sensors can beings installed in the same site or distant (several Km), the introverted data are treated by a unit called processor power station (CPU, PCU, PC...), results are sent in real time to the Men / Machine interfacing that can be a computer with its peripherals (Baily and Wright, 2003).

The SCADA system assures the surveillance and the control of electric, mechanical or electronic equipment equipping all or a part of the network (Munro, 2008). It also allows operators to command and to control all facilities of the power station, as well as to offer all necessary information to the good conduct of a stage data of the power station (Carke et al., 2003; Horng, 2002). The intended role to the SCADA system is to collect data instantaneously of their sites and to transform them in numeric signals by following to send them through the network of communication toward the main and secondary stations (Wiles, 2008). This centralized supervision allows operators, since the control room of the TPP, to control facilities in their domain of exploitation and the different types of incidents (Ozdemir and Karaoc, 2006; Warcuse et al., 1997; Gergely et al., 2010). The center of RADES is equipped of a SCADA network. Stations belong to a network superior Ethernet (10 Mb/s). Mainly this network permits to do exchanges of files between the various stations (Annual Report, 2012). It avoids so the overcharge of the node network bus. Figure 1 shows an overall view of the TPP of RADES using a SCADA system. The SCADA system of the TPP of RADES orders and classifies all data for (Lakhoua, 2009a) (Lakhoua, 2009b) (Lakhoua, 2010a):

(i) Instantaneous impression.
(ii) Visualization on screen using data tables and tabular diagrams.
(iii) Registration of instantaneous exchanges of numeric and analogical data.
(iv) Instantaneous calculation for example corrections of gas debits, direct middle specific consumption, middle values.
(v) Storage of the analogical information of the process.
(vi) Calculation of outputs and losses of the process.
(vii) Surveillance of the SOE signals (entrances rapid contact 1ms)
(viii) Interfacing interactive Men / Machine for the surveillance of the system and the conduct of processes (tabular, curves view of alarm) (Figure 2).

The SCADA system of RADES is equipped of three communication networks (Lakhoua, 2010b):

(i) Field bus, 5 Mbits, permitting to do exchanges of the numeric data of the entrance card / exits (FBM) toward the central system (CP) via modules of communication (FCM);
(ii) Node bus, 10 Mbits, permitting to do exchanges of the numeric data of the central system (CP) via modules of communication (DNBT) toward the Men/Machine interfacing (workstations);
(iii) Ethernet TCP/IP, 100 Mbits, permitting to do exchanges of files between workstations of the Men/Machine interfacing. It avoids so the overcharge of the Nodebus network.

PRESENTATION OF THE INVERSE OSMOSIS AND THE DEMINERALIZATION STATIONS

Considering that the water of the SONEDE contains an

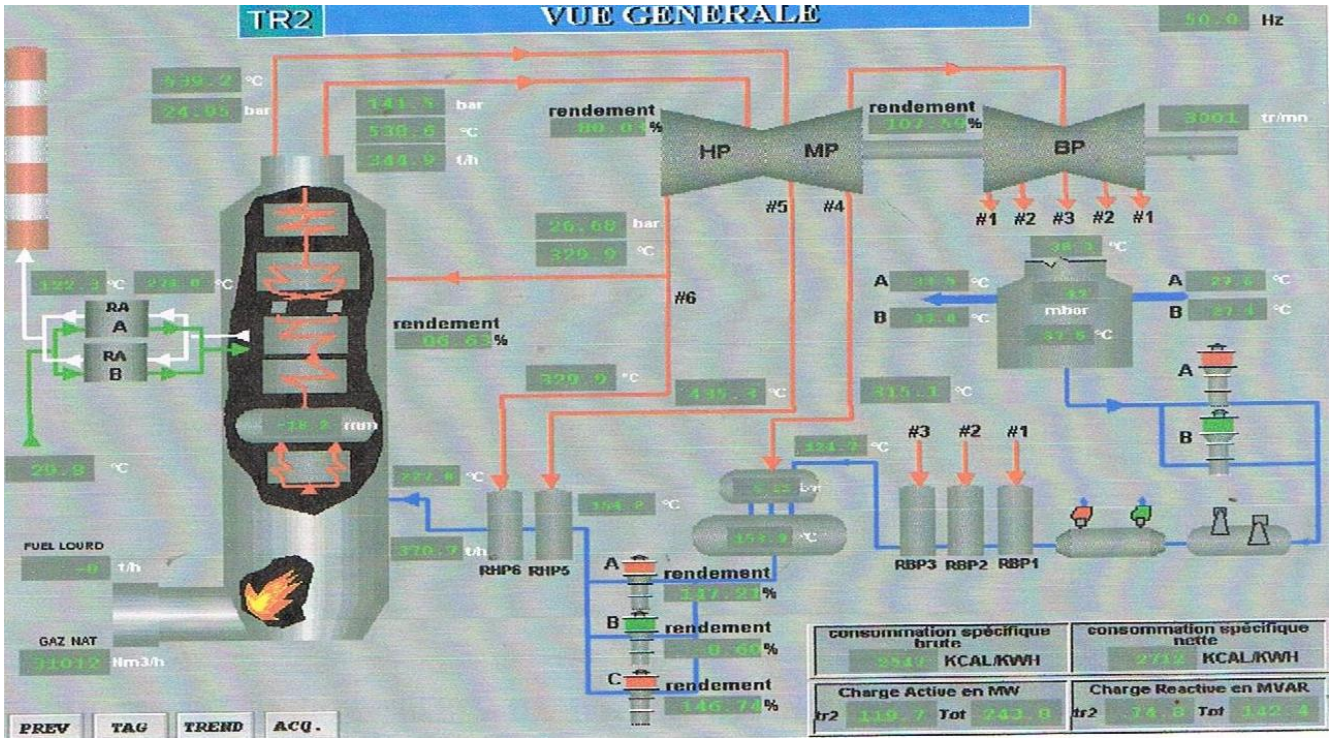

Figure 1. Overall view of the TPP of Radès with SCADA.

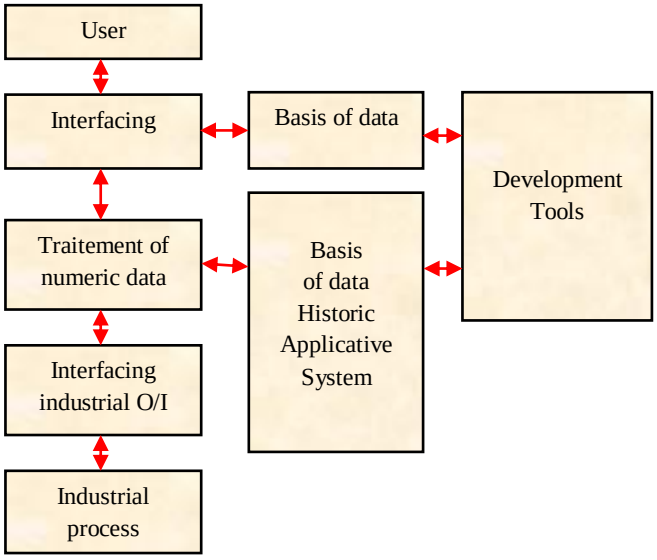

Figure 2. Principle of a SCADA system.

elevated rate in dissolved salts and in matter suspended, it is indispensable to adopt a stage of pretreatment to assure the good working of the inverse osmosis installation and to protect modules against risks of usuries, corrosion and especially membrane calmative (Tarja et al., 2006).

The pretreatment is constituted of two filtration chains each including a sand filter and an active coal filter. Thereafter, we present the two stations of the TPP: inverse osmosis and demineralization.

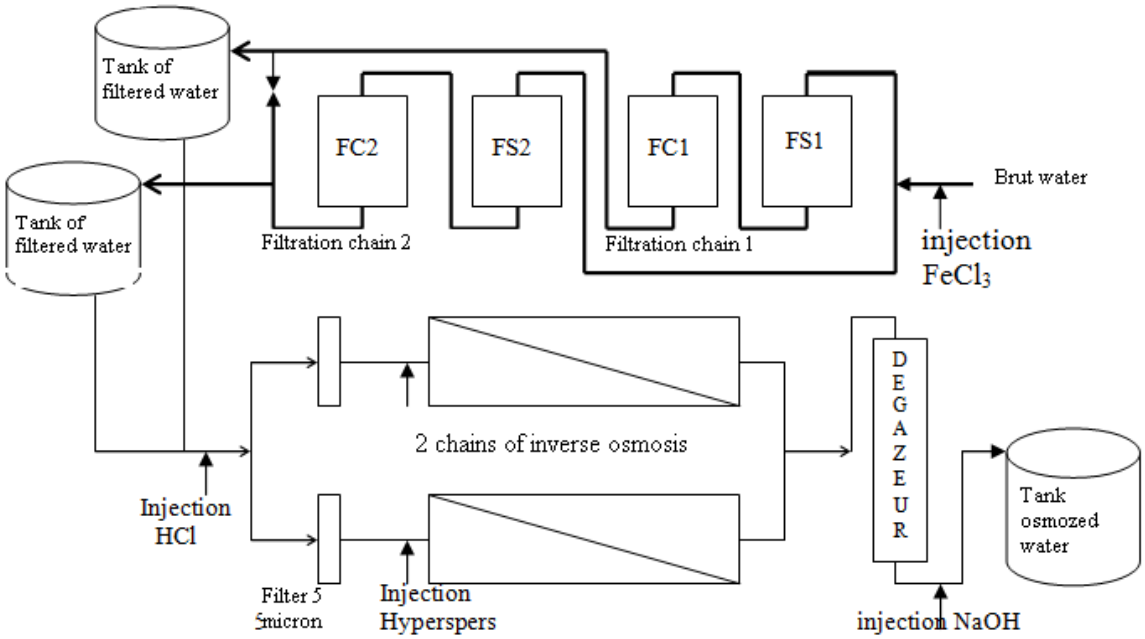

Figure 3. Functional diagram of the inverse osmosis station of the TPP of RADES. FS1: Sand filter of the filtration chain 1. FC1: Active coals filter of the filtration chain 1. FS2: Sand filter of the filtration chain 2. FC2: Active coals filter of the filtration chain 2.

The control of the water quality is an important task to maintain the efficiency and the sure and continuous working of the power station (Yubin et al., 2002). To guarantee the best water quality at the level of the water steam circuit, the TPP of RADES arranges an inverse osmosis station that permits to eliminate the majority of salts dissolved in the raw water before being treated in a demineralization station (Figure 3). This stage serves to minimize risks of failing by corrosion of the turbine or the loss of the efficiency and the power (Electricity and Gas Revue, 2011). The bold lines present the water circuit in the two filtration chains and the light lines present the water circuit in the two inverse osmosis chains. The basic principle of the ion exchange consists in withdrawing ions (remaining salts that are lower to 8%) in solution in water is to recover an ion of value, either to eliminate a harmful or bothersome ion for the ulterior utilization of water (Firoozshahi and Mengyang, 2010). The exchange of ions is a process which ions with a certain load contents in a solution are eliminated of this solution, and replaced in the same way by an equivalent quantity of other ions load gave out by the strong but the opposite load ions are not affected. In the demineralization chain, osmosis water passes by the following stages:

(i) A weak cationic exchanger (CF1);
(ii) A strong cationic exchanger (CF2);
(iii) A weak anionic exchanger (AF1);
(iv) A degasser;
(v) A strong anionic exchanger (AF2);
(vi) A strong cationic exchanger (CF3);
(vii) A strong anionic exchanger (AF3).

After the demineralization, the water must have a lower conductivity of 0.2 µS/cm, a pH between 6.5 and 7.5; silica < 30 ppb. Figure 4 shows the water treatment cycle in the demineralization station.

RESULTS OF THE IDENTIFICATION OF THE WATER LOSS AND THE SCADA APPLICATION

Demineralized water is distributed to the two production plants A and B, the laboratory and the unloading of the fuel station. Consumption of the latter two is negligible compared to the amount consumed by the process of generation of electricity (Figure 5). Demineralized water is distributed to the four stations of the TPP using two tanks. For each station, demineralized water is used primarily for the extra three following circuits:

(i) The water-steam circuit;
(ii) The water cooling circuit of the bodies of various rotating machinery (Noria circuit);
(iii) The secondary steam circuit used primarily for the fuel heating.

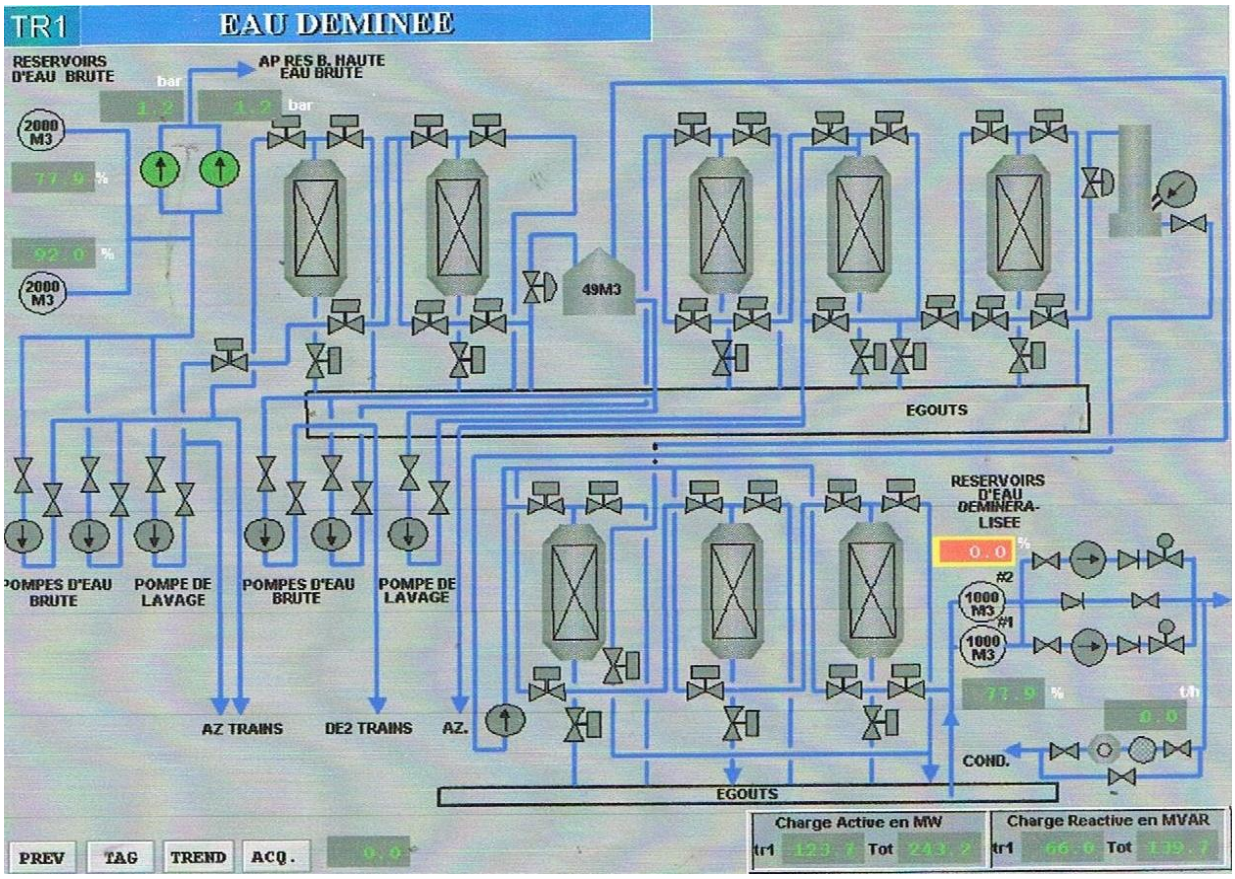

Figure 4. Demineralization station of the TPP of RADES.

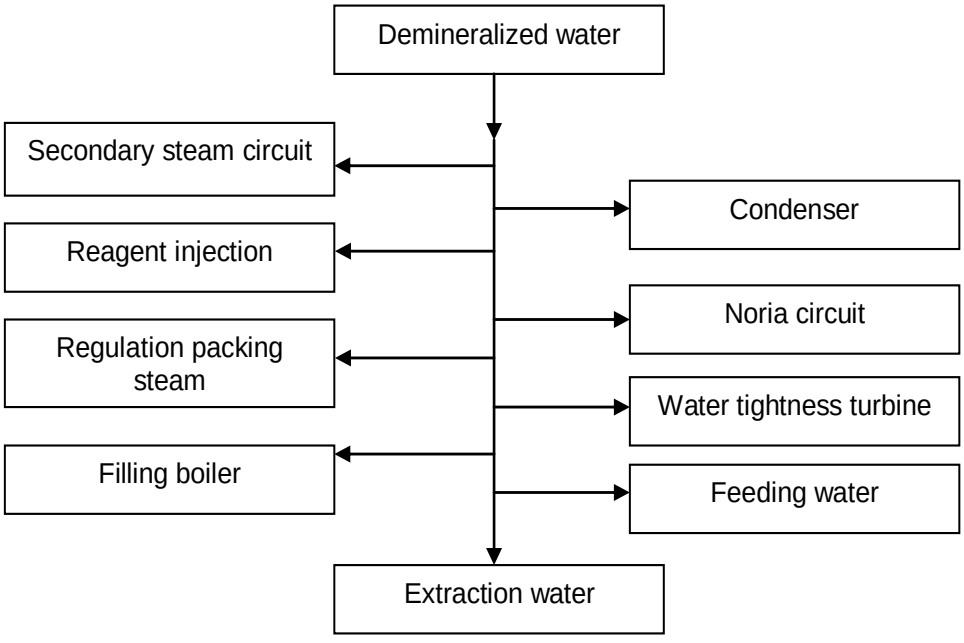

Figure 5. Demineralization station of the TPP.

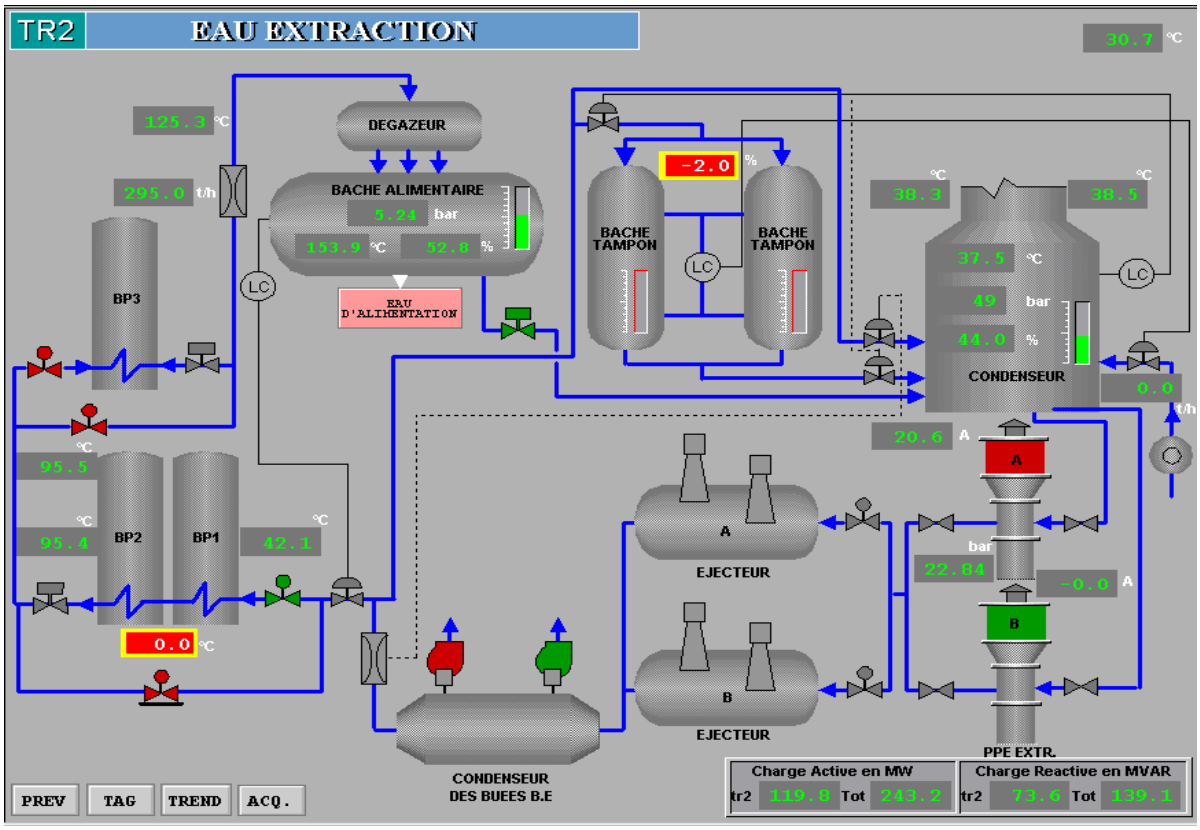

Figure 6. Display of the water extraction circuit of the TPP.

The ongoing purges are formed by the boiler purges which are necessary to maintain the quality of condenser water steam cycle. The ongoing purges volume varies between 50 and 70 m^3/day for one station. Sampling purges are carried out automatically by on line continuously analyses of the water of the boiler parameters (pH, conductivity...). The volume of these purges varies between 3 and 5 m^3/day for one station. The staple purges occur after judgments or in case of anomalies that require draining of the boiler or other bodies (ball boiler, covering food...). The sampling purges of the plant A allow extra Noria circuits of the two stations. The make-up of the water steam circuit varies between 70 and 80 m^3/day for one station.

In this application, we have installed an ultrasonic flow meter in the make-up water circuit and an electromagnetic flow meter in the osmosis position. Flow converted to the level of the ultrasonic flow meter will be issued as an electric signal 4 to 20 mA, towards the electronic room to treat by the input (UA 374 and UT 375) modules. Then, it will be forwarded to the ordinary and finally visualized in the control room. Figure 6 shows the display of the circuit of the water extraction of the TPP.

This application is declined in six stages:

Stage 1: Choosing the site of the signal (FBM module) that treats the demineralized water.
Stage 2: Programming the AIN block for the supervision of the ultrasonic flow meter signals.
Stage 3: Testing the AIN block by injection of current.
Stage 4: Passing the cable between the electronic room and the SCADA room.
Stage 5: Programming three ACCUM blocks and two COUT blocks.
Stage 6: Improving the existing tabular of the water extraction circuit.

CONCLUSION

SCADA systems are used to control and monitor physical processes, examples of which are transmission of electricity, transportation of gas and oil in pipelines, water distribution, traffic lights, and other systems used as the basis of modern society. In this paper, we presented an identification of the water loss in a thermal power plant and an application of the SCADA system on the water extraction circuit. Moreover, we proved the importance on using a SCADA system for sustainable development in

the supervision of the thermal power plants. Also the paper outlines the general concepts and required equipments for the supervision of such power plants. Some applications of SCADA system implementation in electrical companies over the world have been presented.

Conflict of Interest

The author(s) have not declared any conflict of interests.

REFERENCES

Annual Report (2012). Tunisian Society of Electricity and Gas. Tunisia.

Baily D, Wright E (2003). Practical SCADA for Industry. Elsevier. http://store.elsevier.com/Practical-SCADA-for-Industry/David-Bailey/isbn-9780750658058/

Carke G, Rynders D, Wright E (2003). Practical Modern SCADA Protocols. Elsevier.

Changling L, Boon-Teck O (2006). Frequency deviation of thermal power plants due to wind farms, IEEE Trans. Energy Conver. 21(3):708-716. http://dx.doi.org/10.1109/TEC.2006.874210

Ecob D, Williamson J, Hughes G, Davis J (1995). PLC's and SCADA - a water industry experience. IEE Colloquium on Application of Advanced PLC Systems with Specific Experiences from Water Treatment. pp. 601-610. http://dx.doi.org/10.1049/ic:19950742

Electricity and Gas Revue (2011). Tunisian Society of Electricity and Gas. N°16. Tunisia.

Firoozshahi A, Mengyang L (2010). Water treatment plant intelligent monitoring in large gas refinery. IEEE International Conference on Computational Technologies in Electrical and Electronics Engineering. pp. 785-789.

Gergely EI, Coroiu L, Popentiu-Vladicescu F (2010). Analysis of the influence of the programming approach on the response time in PLC Control Programs, JCSCS. 3(1):61-64.

Horng JH (2002). SCADA system of DC motor with implementation of fuzzy logic controller on neural network. Adv. Eng. Software. pp. 361–364. http://dx.doi.org/10.1016/S0965-9978(02)00020-0

Kagiannas AG, Askounis D, Anagnostopoulos K, Psarras J (2003). Energy policy assessment of the Euro-Mediterranean cooperation, Energy Conver. Manage. pp. 2665-2686.

Lakhoua MN (2009a). Methodology for designing supervisory production systems: Case study of a counting system of natural gas, J. Elect. Eng. 9(N°3).

Lakhoua MN (2009b). Application of functional analysis for the design of supervisory systems: Case study of heavy fuel-oil tanks. Int. Trans. Syst. Sci. Applications. 5(N°1):21-33.

Lakhoua MN (2010a). Surveillance of pumps vibrations using a SCADA. Control Eng. Appl. Informatics. 12(N°1).

Lakhoua MN (2010b). SCADA applications in thermal power plants. Int. J. Phys. Sci. 5(N°7):1175-1182.

Munro K (2008). SCADA - A critical situation, Network Security. 1:4-6. http://dx.doi.org/10.1016/S1353-4858(08)70005-9

Ozdemir E, Karacor M (2006). Mobile phone based SCADA for industrial automation. ISA. Trans. 45(N°1):67-75. http://dx.doi.org/10.1016/S0019-0578(07)60066-4

Tarja AM, Ungureanu G, Capajana D, Covaciu FA (2006). SCADA System for Water Potential Management of a Hydropower Plants Cascade. IEEE Int. Conf. Automation. Quality Testing. Robotics. 1:410-414.

Vitaly A (2008). Alternative trends in development of thermal power plants. Appl. Thermal Eng. 28(2-3):190-194. http://dx.doi.org/10.1016/j.applthermaleng.2007.03.025

Warcuse J, Menz B, Payne JR (1997). Servers in SCADA applications. IEEE Trans. Ind. Appl. 9-2:1295-1334.

Wiles J (2008). Techno Security's Guide to Securing SCADA: A Comprehensive Handbook on Protecting the Critical Infrastructure. Elsevier. http://store.elsevier.com/Techno-Securitys-Guide-to-Securing-SCADA/Jack-Wiles/isbn-9780080569994/

Yubin X, Yinzhang G, Honggang W, Jianchao Z (2002). Distributed control system in water plant based on ControlNet. Proceedings of the 4th World Congress on Intelligent Control and Automation. 4:3113-3117.

academicJournals

Vol. 9(10), pp. 250-254, 30 May, 2014
DOI: 10.5897/IJPS2014.4120
ISSN 1992 - 1950
Article Number: 736CEBB45016

http://www.academicjournals.org/IJPS

International Journal of Physical Sciences

Full Length Research Paper

Simulation analysis of the effect graded Zn(O,S) on the performance of the ultra thin copper indium gallium diselenide (CIGS) solar cells

Chihi Adel*, Boujmil Mohamed Fethi and Bessais Brahim

Laboratoire Photovoltaïque, Centre des Recherches et des Technologies de l'Energie Technopole BorjCedria B.P No. 95 2050 - Hammam Lif - Tunisie.

Received 31 January, 2014; Accepted 12 May, 2014

This paper indicated a numerical modeling of ultra thin copper indium gallium diselenide (CIGS) solar cells. An optimum value of the thickness of the structure has been calculated and it is shown that by optimizing the thickness of the cell, efficiency has been increased and cost of production can been reduced. Numerical optimizations have been done by adjusting parameters such as thickness of the layers and the gap. It shows that by optimization of the considered structure, open circuit voltage (V_{co}) increases and an improvement of conversion efficiency has been observed in comparison to the conventional CIGS system.

Key words: Graded pseudo copper indium gallium diselenide (CIGS)-Zn(O,S), solar cells, efficiency enhancement, solar capacitance simulator (SCAPS).

INTRODUCTION

Copper indium gallium diselenide ($CuIn_{1-x}Ga_xSe_2$ or CIGSe) solar cells is a multilayer thin film technology which has been increasingly developed in the last decade; thanks to its relatively low cost combined with high efficiencies. CIGSe is a direct band gap semiconductor with a chalcopyrite structure, a p-type doping and band gap varying continuously with the gallium content x from about 1 eV for pure Cis to about 1.7 eV for CuGaSe. Presently, the highest conversion efficiency never reported in thin film technology, with a record value of 20.3% was recently reported by Zentrum für Sonnenenergie- und Wasserstoff-Forschung Baden-Württemberg (Centre for Solar Energy and Hydrogen Research) (ZSW) (Jackson et al., 2011). Over the past decade, the CIGSe field experienced an increasing industrial development with the commercialization of high efficiency modules (Powalla et al., 2006). It is now considered as one of the most promising alternative technology to silicon-based solar cells. The p-CIGSe layer can be grown by several vacuum and non vacuum methods, such as co-evaporation (Repins et al., 2008; Thornton, 1984), sputtering (Thornton, 1984; Nakada et al., 1995), ectrodeposition (Lincot et al., 2004) or nano-particles based techniques ()Vijay et al., 2003).

A numerical device model for the electronic and optical processes allows researchers for a good understanding

*Corresponding author. E-mail: supereagle2791@yahoo.fr

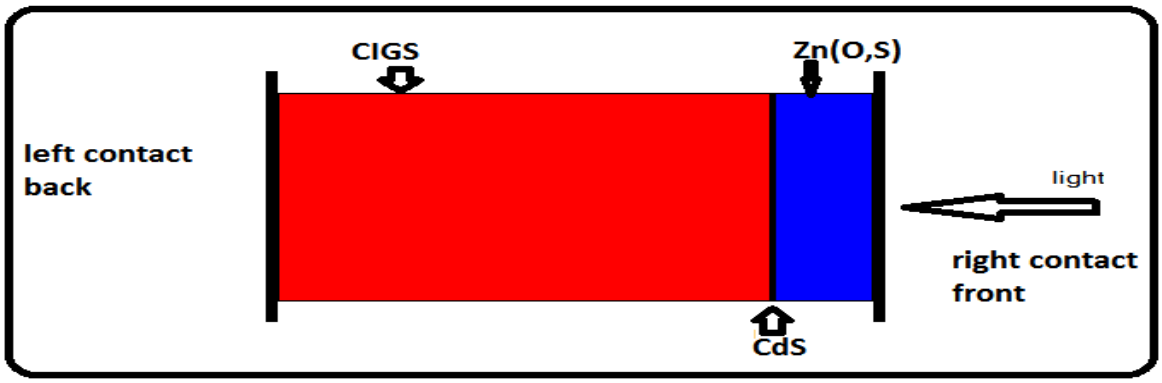

Figure 1. Schematic structure of CIGS based thin film solar cells.

and also, efficient optimization of thin film solar cells. There were several numerical studies for investigation of thin film solar cells that reports to investigate most important parameters of cells such as grain boundary, defects density and thickness which contribute in performance of thin film solar cell.

Several numerical software have been developed by research groups to predict the thin film solar cell performance of the cell, a typical CIGS solar cell structure which composed of three layers, namely a transparent conductive oxide (TCO) contact which composed of n-doped graded Zn(O,S), n-doped CdS buffer layer, and p-doped $CuIn_{1-x}Ga_xSe_2$ layer.

In this paper, in order to investigate the effects of cell composed layers thickness on the performance of the cell, a typical CIGS structure which composed of five layers grille/graded Zn(O,S) / CdS / graded CIGSe / Metalas is shown in Figure 1.

The aim of this article is to illustrate the effects of band gap grading in $Cu(In,Ga)Se_2$ absorber or CIGSe and in Zn(O,S) the purpose is to demonstrate that solar capacitance simulator (SCAPS) can handle such complicated structure.

NUMERICAL SIMULATION METHODOLOGY

In this study, numerical modeling of CIGS thin films solar cell has been carried out by SCAPS-1D, version 3.2.01 computer software to investigate the effects on absorber band gap grading on the overall CIGS solar cell device performance. SCAPS is a one-dimensional solar cell simulation program developed at the department of Electronics and Information Systems (ELIS) of the University of Gent.

Several researchers have contributed to its development (Burgelman et al., 2000; Decock et al., 2011). This version have several features such as almost all parameters can be graded (that is, dependent on the local composition or on the depth in the cell) : E.g, χ, ε, NC, NV, v_{thn}, v_{thp}, μ_n, μ_p, N_A, N_D, all traps (defects)N_t.
Poisson equation used for semiconductor device:

$$\frac{\partial}{\partial x}\left(\varepsilon_r \varepsilon_0 \frac{\partial}{\partial x}\Psi(x)\right) = q\left(p(x) - n(x) + N_D - N_A + \rho_{def}\right) \quad (1)$$

Where Ψ is electrostatic potential, q is charge of electron, ε_r and ε_0 are the relative and the vacuum permittivity, respectively, p and n are hole and electrons concentrations, N_D is charge impurities of donor and N_A is acceptor type, ρ_{def} is the defect distribution .
The continuity equations for electrons and holes are:

$$-\frac{\partial}{\partial x}J_n(x) + G(x) - R(x) = \frac{\partial n}{\partial t} \quad (2)$$

$$-\frac{d}{dx}J_p(x) + G(x) - R(x) = \frac{\partial p}{\partial t} \quad (3)$$

Where

$$j_n = -\frac{\mu n}{q}\, n\, \frac{\partial E_{Fn}}{\partial x} \quad (4)$$

$$j_p = \frac{\mu p}{q}\, p \frac{\partial E_{Fp}}{\partial x} \quad (5)$$

Where J_n and J_p are electron and hole current densities, E_{Fn} and E_{Fp} are Quasi-Fermi level for electrons and holes, G(x) and R(x) are charge generation and recombination rates. The system of equations described that Equations 1, 2 and 3 are solved numerically, using a Gummel iteration scheme with Newton Raphson substeps (Niemegeers et al., 1998; Selberherr, 1984).

SCAPS calculates solution of the basic semiconductor equations in one-dimensional and in steady state conditions.

Recombination in deep bulk levels and their occupation is described by the Shockley Read Hall (SRH) formalism. The current transport mechanism of our model can be explained in general terms by considering the effect of light on the band diagram.

Since the calculations require the input of device parameters, the surface recombination velocities of both electrons and holes were set at 10^7 cm/s. The solar AM 1.5 radiation was adopted as the illuminating source with power density of 100 mW/cm^2. The light refection of the front and back contacts was set at 0.1 and 1, respectively. The light absorption coefficient for CIGS layer was taken from absorption file. The other simulating parameters are given in Table 1.

RESULTS AND DISCUSSION

This paper indicates a study to optimize the CIGS based solar cell by considering the effects of layer thickness on

Table 1. Summary of the input parameters of the SCAPS demonstration model. The contacts are ohmic ('flat band').

Parameter	Graded p-CIGS	CdS	Graded n- Zn(O,S)
ε_r	13.6	10	9
χ (eV)	4.5	4.2	4.45
Eg(eV)	1.04 - 1.68	2.4	3.6
μ_n(cm^2/Vs)	100	100	100
μ_p (cm^2 /Vs)	100	25	25
N_c (cm^{-3})	2.2×10^{18}	2.2×10^{18}	2.2×10^{18}
N_v(cm^{-3})	1.8×10^{18}	1.8×10^{19}	1.8×10^{19}
N_A(cm^{-3})	2×10^{18}	1	10^{17}
N_D(cm^{-3})	1	10^{16}	1
Ve (cm /s)	10^7	10^7	10^7
V_h(cm /s)	10^7	10^7	10^7

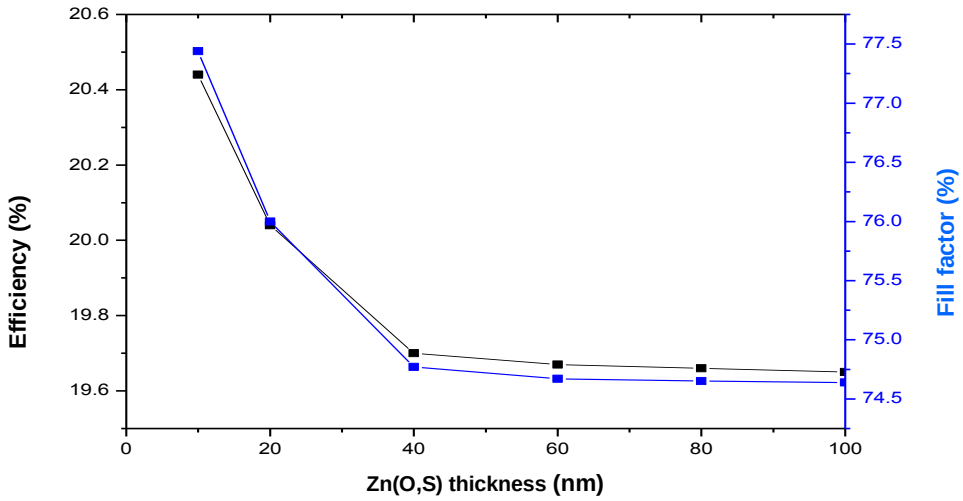

Figure 2. Variation efficiency and FF as a function of graded Zn(O,S) thickness.

the performance of the cell and the graded structure of Zn(O,S). In this respect, the structure of CIGS based thin film solar cell is shown in Figure 1. Figure 2 shows variation of TCO thickness Zn(O,S) versus fill factor (FF) and efficiency. It is shown that by decreasing the thickness of graded n-Zn(O,S), cell efficiency increases. It is due to this fact that n-Zn(O,S) is not fully transparent for light and this layer absorbs and reflects the sunlight. As it is shown in Figure 2 by increasing the Zn(O,S) thickness, light absorption increases and leads to lower efficiency. By decreasing the Zn(O,S) layer from 100 nm to 10 nm, cell efficiency increases from about 19.60 to 20.44; also FF curve has the same increasing rate as it shown in η. Calculation shows that variation of the Zn (O,S) thickness has no effect on the current density.

Figure 3 shows the variation of short circuit current (J_{sc}) and open circuit voltage (v_{oc}) interms of the graded p-CIGS. It is shown that by increasing the thickness from 2 nm to 3 µm, J_{sc} increases and after about 1 µm is constant. Also, Figure 3 demonstrates that by increasing the thickness from 2 nm to 3 µm, V_{oc} decreases exponentially.

Figure 4 shows the variation of η efficiency and FF versus CIGS thickness. It is shown that by increasing the thickness from 10 nm to 0.5 µm, efficiency increases from 18.30 to 20.04; efficiency increases about 10% and after 0.5 µm falls down. From the simulation, results were found that the optimized value of the graded p-CIGS is 0.5 µm which leads to a thinner and cheaper solar cell. Simulation results shows optimized value of CIGS and graded n-Zn(O,S) thickness is 0.5 µm and 10 nm, respectively. By choosing the optimized value J_{sc}, V_{oc} and η are 41.85 mA/cm^2, 0.63 V and 20.44%, respectively. From Figure 5, it is clear that in optimized structure V_{oc} increased, J_{sc} decreases a little but cell efficiency increases from 18.35 to 20.04.

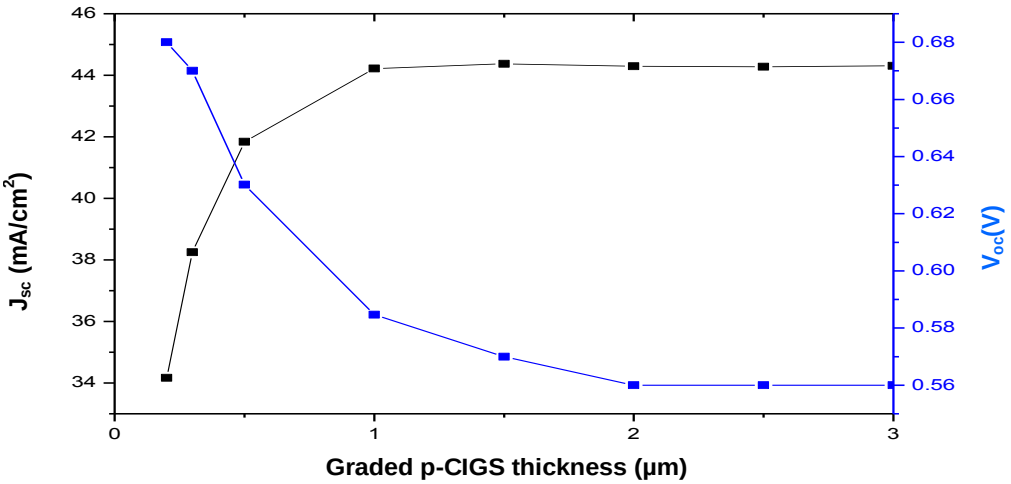

Figure 3. Variation of J_{sc} and V_{oc} as a function of graded CIGS thickness.

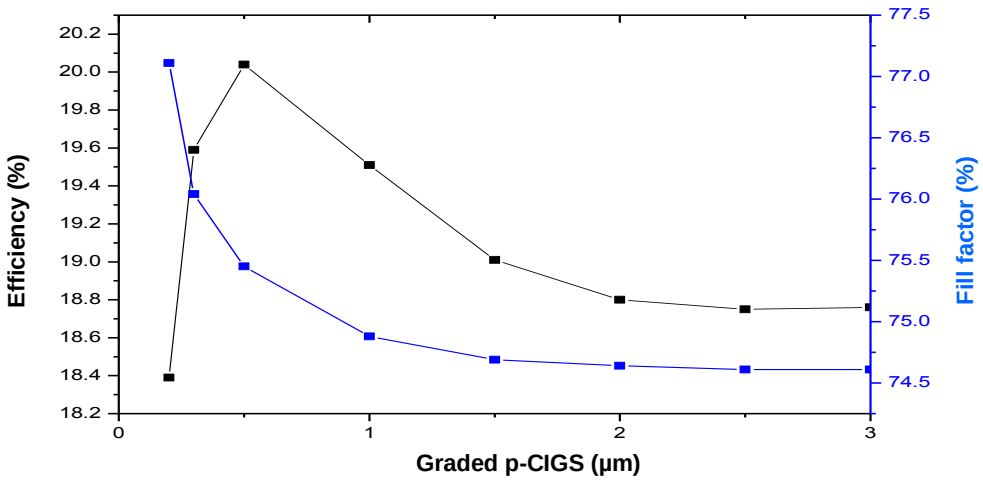

Figure 4. Variations of efficiency and FF as a function of graded CIGS thickness.

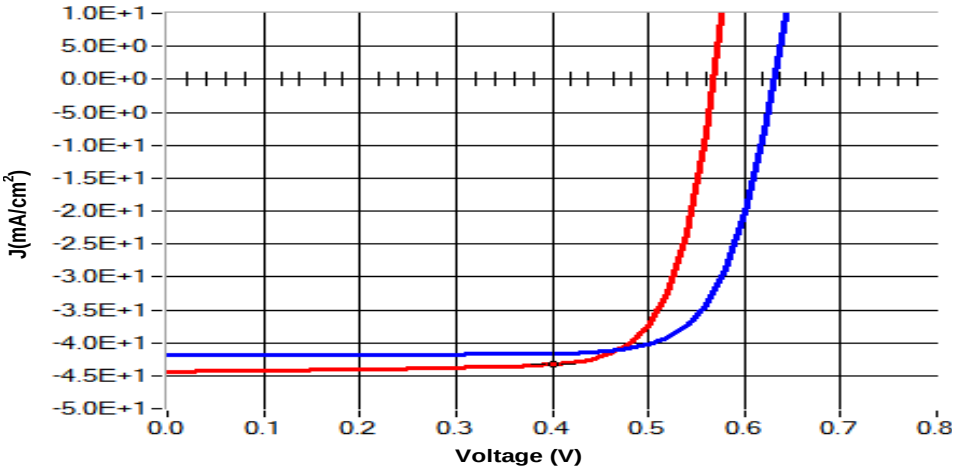

Figure 5. J-V characteristics of typical (red curve) and optimized (blue curve) graded CIGS.

Conclusion

This paper indicated a numerical investigation of graded CIGS based solar cells. Numerical optimizations have been done by adjusting parameters such as the combination of band gap,as well as the specific structure of the cell. From the simulation result, it was found that by optimization of the considered structure, optimized value of CIGS and TCO thickness is 0.6 um and 10 nm and an improvement of conversion efficiency has been observed in comparison to the conventional CIGS which cell efficiency increases from 18.04 to 20.04%.

Conflict of Interests

The author(s) have not declared any conflict of interests

ACKNOWLEDGMENT

The authors gratefully acknowledge Dr. Marc Burgelman, University of Gent, for providing the SCAPS simulation software.

REFERENCES

Jackson P (2011). New world record efficiency for Cu(In,Ga)Se2 thin film solar cells beyond 20%. Progress in Photovoltaics: Res. Appl. 19:894–897. http://dx.doi.org/10.1002/pip.1078

Powalla M (2006). Large-area CIGS modules: Pilot line production and new developments. Solar Ener. Mater. Solar Cells 90:3158–3164. http://dx.doi.org/10.1016/j.solmat.2006.06.052

Repins I, Contreras MA, Egaas B, DeHart C, Scharf J, Perkins CL, To B, Noufi R (2008). 19•9% efficient ZnO/CdS/CuInGaSe2solar cell with 81•2% fill factor. Progress in Photovoltaics: Res. Appl. 16:235–239. http://dx.doi.org/10.1002/pip.822

Thornton JA (1984). Reactive sputtered copper indium diselenide films for photovoltaic applications. J. Vac. Sci. Technol. A: Vacuum, Surfac. Films. 2:307.

Nakada T, Migita K, Niki S. AkioKunioka (1995). Microstructural characterization for sputter-deposited CuInSe films and photovoltaic devices. Japanese J. Appl. Phys. 34:4715–4721. http://dx.doi.org/10.1143/JJAP.34.4715

Lincot D (2004). Chalcopyrite thin film solar cells by electrodeposition. Solar Energy 77:725–737. http://dx.doi.org/10.1016/j.solener.2004.05.024

Vijay K (2003). Ashish Bansal, Phucan Le, Omar Asensio.Non-vacuum processing of CuIn1−xGaxSe2 solar cells on rigid and flexible substrates using nanoparticle precursor inks. Thin Solid Films 431-432:53–57. http://dx.doi.org/10.1016/S0040-6090(03)00253-0

Burgelman M, Nollet P, Degrave S (2000). Modelling polycrystalline semiconductor solar cells, Thin Solid Films, 361:527-532. http://dx.doi.org/10.1016/S0040-6090(99)00825-1

Decock K, Khelifi S, Burgelman M (2011). Modelling multivalent defects in thin film solar cells, Thin Solid Films, 519:7481-7484. http://dx.doi.org/10.1016/j.tsf.2010.12.039

Niemegeers A Gillis S, Burgelman MA (1998). User program for realistic simulation of polyrystallineheterojunction solar cells: SCAPS-1D, Proceedings of the 2nd World Conference on Photovoltaic Energy Conversion, Wien, pp. 672-675.

Selberherr S (1984). Analysis and simulation of semiconductor devices. Springer Verlag Wien-New York, http://dx.doi.org/10.1007/978-3-7091-8752-4

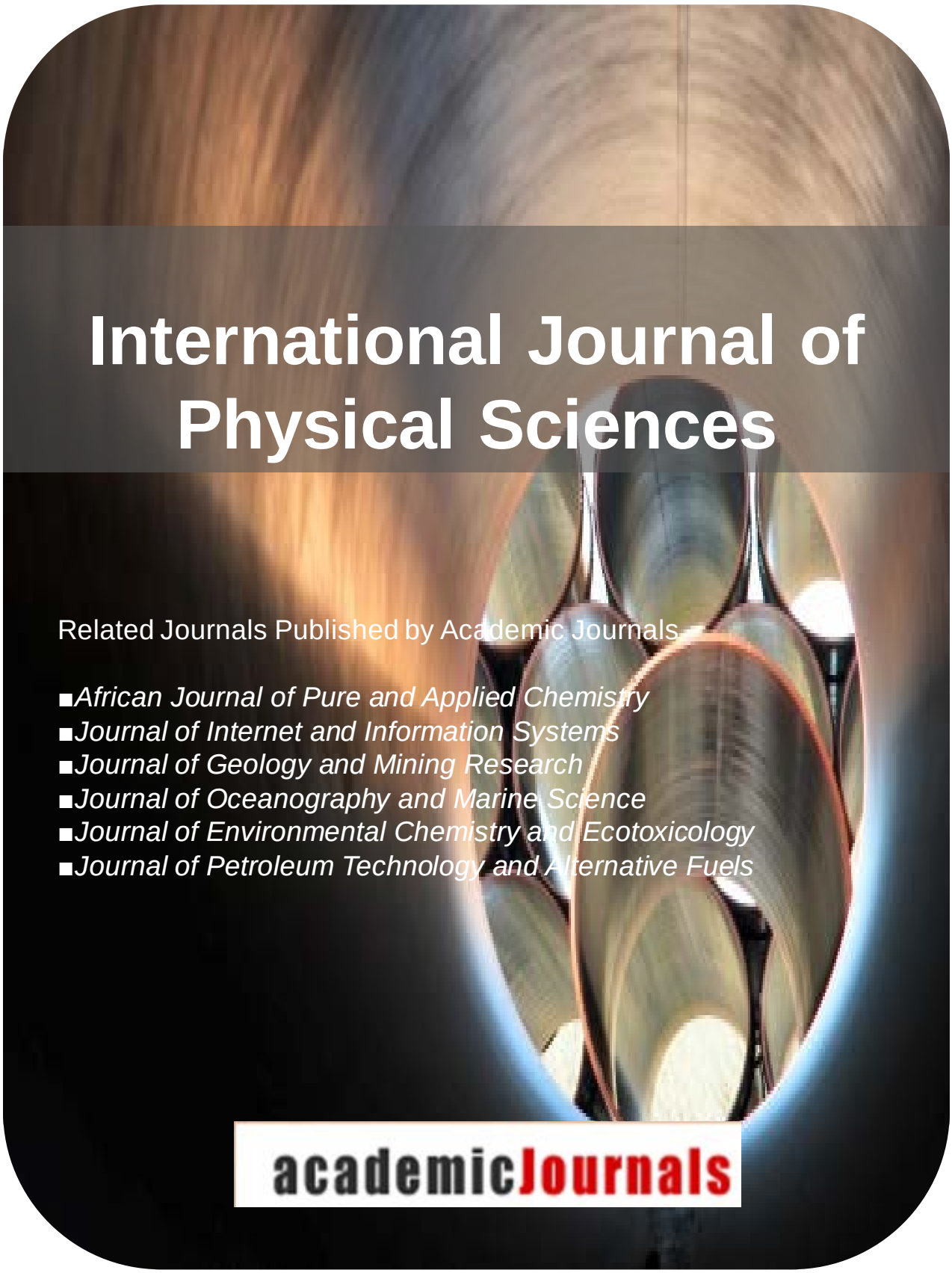

International Journal of Physical Sciences

Related Journals Published by Academic Journals

- *African Journal of Pure and Applied Chemistry*
- *Journal of Internet and Information Systems*
- *Journal of Geology and Mining Research*
- *Journal of Oceanography and Marine Science*
- *Journal of Environmental Chemistry and Ecotoxicology*
- *Journal of Petroleum Technology and Alternative Fuels*

academicJournals